

# The Heavy Photon Search Test Detector

M. Battaglieri<sup>a</sup>, S. Boyarinov<sup>b</sup>, S. Bueltmann<sup>c</sup>, V. Burkert<sup>b</sup>, A. Celentano<sup>a</sup>, G. Charles<sup>f</sup>, W. Cooper<sup>d</sup>, C. Cuevas<sup>b</sup>, N. Dashyan<sup>e</sup>, R. DeVita<sup>a</sup>, C. Desnault<sup>f</sup>, A. Deur<sup>b</sup>, H. Egriyan<sup>b</sup>, L. Elouadrhiri<sup>b</sup>, R. Essig<sup>g</sup>, V. Fadeyev<sup>h</sup>, C. Field<sup>i</sup>, A. Freyberger<sup>b</sup>, Y. Gershtein<sup>j</sup>, N. Gevorgyan<sup>e</sup>, F.-X. Girod<sup>b</sup>, N. Graf<sup>i</sup>, M. Graham<sup>i</sup>, K. Griffioen<sup>k</sup>, A. Grillo<sup>h</sup>, M. Guidal<sup>f</sup>, G. Haller<sup>i</sup>, P. Hansson Adrian<sup>i,\*</sup>, R. Herbst<sup>i</sup>, M. Holtrop<sup>l</sup>, J. Jaros<sup>i</sup>, S. Kaneta<sup>b</sup>, M. Khandaker<sup>m</sup>, A. Kubarovsky<sup>n</sup>, V. Kubarovsky<sup>b</sup>, T. Maruyama<sup>i</sup>, J. McCormick<sup>i</sup>, K. Moffeit<sup>i</sup>, O. Moreno<sup>h</sup>, H. Neal<sup>i</sup>, T. Nelson<sup>i</sup>, S. Niccolai<sup>f</sup>, A. Odian<sup>i</sup>, M. Oriunno<sup>i</sup>, R. Paremuzyan<sup>e</sup>, R. Partridge<sup>i</sup>, S. K. Phillips<sup>l</sup>, E. Rauly<sup>f</sup>, B. Raydo<sup>b</sup>, J. Reichert<sup>j</sup>, E. Rindel<sup>f</sup>, P. Rosier<sup>f</sup>, C. Salgado<sup>m</sup>, P. Schuster<sup>o</sup>, Y. Sharabian<sup>b</sup>, D. Sokhan<sup>p</sup>, S. Stepanyan<sup>b</sup>, N. Toro<sup>o</sup>, S. Uemura<sup>i</sup>, M. Ungaro<sup>b</sup>, H. Voskanyan<sup>e</sup>, D. Walz<sup>i</sup>, L. B. Weinstein<sup>c</sup>, B. Wojtsekhowski<sup>b</sup>

<sup>a</sup>Istituto Nazionale di Fisica Nucleare, Sezione di Genova e Dipartimento di Fisica dell'Università, 16146 Genova, Italy

<sup>b</sup>Thomas Jefferson National Accelerator Facility, Newport News, Virginia 23606

<sup>c</sup>Old Dominion University, Norfolk, Virginia 23529

<sup>d</sup>Fermi National Accelerator Laboratory, Batavia, IL 60510-5011

<sup>e</sup>Yerevan Physics Institute, 375036 Yerevan, Armenia

<sup>f</sup>Institut de Physique Nucléaire, CNRS/IN2P3 and Université Paris Sud, Orsay, France

<sup>g</sup>Stony Brook University, Stony Brook, NY 11794-3800

<sup>h</sup>Santa Cruz Institute for Particle Physics, University of California, Santa Cruz, CA 95064

<sup>i</sup>SLAC National Accelerator Laboratory, Menlo Park, CA 94025

<sup>j</sup>Rutgers University, Department of Physics and Astronomy, Piscataway, NJ 08854

<sup>k</sup>The College of William and Mary, Department of Physics, Williamsburg, VA 23185

<sup>l</sup>University of New Hampshire, Department of Physics, Durham, NH 03824

<sup>m</sup>Norfolk State University, Norfolk, Virginia 23504

<sup>n</sup>Rensselaer Polytechnic Institute, Department of Physics, Troy, NY 12181

<sup>o</sup>Perimeter Institute, Ontario, Canada N2L 2Y5

<sup>p</sup>University of Glasgow, Glasgow, G12 8QQ, Scotland, UK

---

## Abstract

The Heavy Photon Search (HPS), an experiment to search for a hidden sector photon in fixed target electroproduction, is preparing for installation at the Thomas Jefferson National Accelerator Facility (JLab) in the Fall of 2014. As the first stage of this project, the HPS Test Run apparatus was constructed and operated in 2012 to demonstrate the experiment's technical feasibility and to confirm that the trigger rates and occupancies are as expected. This paper describes the HPS Test Run apparatus and readout electronics and its performance. In this setting, a heavy photon can be identified as a narrow peak in the  $e^+e^-$  invariant mass spectrum above the trident background or as a narrow invariant mass peak with a decay vertex displaced from the production target, so charged particle tracking and vertexing are needed for its detection. In the HPS Test Run, charged particles are measured with a compact forward silicon microstrip tracker inside a dipole magnet. Electromagnetic showers are detected in a PbWO<sub>4</sub> crystal calorimeter situated behind the magnet, and are used to trigger the experiment and identify electrons and positrons. Both detectors are placed close to the beam line and split top-bottom. This arrangement provides sensitivity to low-mass heavy photons, allow clear passage of the unscattered beam, and avoids the spray of degraded electrons coming from the target. The discrimination between prompt and displaced  $e^+e^-$  pairs requires the first layer of silicon sensors be placed only 10 cm downstream of the target. The expected signal is small, and the trident background huge, so the experiment requires very large statistics. Accordingly, the HPS Test Run utilizes high-rate readout and data acquisition electronics and a fast trigger to exploit the essentially 100% duty cycle of the CEBAF accelerator at JLab.

**Keywords:** silicon, microstrip, tracking, vertexing, heavy photon, dark photon, electromagnetic calorimeter

---

## 1. Introduction

The heavy photon ( $A'$ ), aka a “hidden sector” or “dark” photon, is a massive gauge boson which couples weakly to electric charge by mixing with the Standard Model photon [1, 2]. Consequently, it can be radiated by electrons and subsequently decay into  $e^+e^-$  pairs, albeit at rates far below those of QED trident processes. Heavy photons have been suggested by numerous beyond Standard Model theories [3] to explain the discrepancy between theory and experiment of the muon’s  $g-2$  [4], and as a possible explanation of recent astrophysical anomalies, e.g. [5, 6, 7]. Heavy photons couple directly to hidden sector particles with “dark” or “hidden sector” charge; these particles could constitute all or some of the dark matter, e.g. [8, 9]. Current phenomenology highlights the  $20 - 1000 \text{ MeV}/c^2$  mass range, and suggests that the coupling to electric charge,  $\epsilon e$ , has  $\epsilon$  in the range of  $10^{-3} - 10^{-5}$ . This range of parameters makes  $A'$  searches viable in medium energy fixed target electroproduction [10], but requires large data sets and good mass resolution to identify a small mass peak above the copious QED background. At small couplings, the  $A'$  becomes long-lived, so detection of a displaced decay vertex can reject the prompt QED background and boost experimental sensitivity.

The HPS experiment [11] is preparing for installation in Hall-B at JLab in the Fall of 2014 to search for heavy photons by directing the 2.2-6.6 GeV CEBAF12 electron beam onto a thin ( $0.25\% X_0$ ) Tungsten target foil. The HPS experiment uses both invariant mass and secondary vertex signatures to search for  $A'$  decays into  $e^+e^-$  pairs. At CEBAF energies, the  $A'$  decay products are boosted along the beam axis with small opening angles. For couplings  $\epsilon \ll 10^{-3}$ ,  $A'$  decay lengths range from millimeters to tens of centimeters and beyond. Accordingly the tracking detectors cover opening angles down to 15 mrad and are placed just 10 cm downstream of the target.

HPS employs a 90 cm long silicon tracking and vertexing detector located inside a dipole magnet to measure momenta and decay vertex positions. A fast PbWO<sub>4</sub> electromagnetic calorimeter downstream of the magnet provides the trigger and electron identification. Both the silicon tracker and the ECal have  $\sim\text{ns}$  timing resolution, which eliminates much of the out-of-time background from multiple scattered beam electrons. Fast front end electronics and high trigger and

data rate capability and the effectively 100% duty cycle of the CEBAF accelerator allows HPS to accumulate the very large statistics needed to be sensitive to the highly suppressed production of heavy photons.

The HPS Test Run, using a simplified version of the HPS apparatus, was proposed and approved at JLab as the first stage of HPS. Its purposes included demonstrating that the apparatus and data acquisition systems are technically feasible and the trigger rates and occupancies to be encountered in electron-beam running are as simulated. Given dedicated running time with electron beams, the HPS Test Run apparatus is capable of searching for heavy photons in unexplored regions of parameter space. Therefore, key design criteria and requirements for HPS and the HPS Test Run apparatus are the same:

- uniform acceptance between 15 and approximately 70 mrad in the forward region to catch boosted decay products close to the beam,
- beam passage through the apparatus in vacuum, to eliminate direct interactions with the detector and minimize beam gas interactions,
- detector components that can survive and efficiently operate in a high radiation environment with some localized doses at the 100 Mrad level,
- high-rate electronics, handling trigger rates up to 50 kHz and data rates of 100 MB/s to permanent storage,
- a flexible, redundant and efficient trigger for selecting electron and positron pairs, capable of handling rates up to 50 kHz,
- hit reconstruction efficiency higher than 99% and average track reconstruction efficiency higher than 98% for electrons and positrons,
- 2 ns hit time resolution in the silicon vertex tracker,
- $A'$  mass resolution of 2.5% or better, which translates to momentum resolution of 4.5% and angular resolution of 2 mrad/ $p(\text{GeV}/c)$  for  $B=0.5 \text{ T}$ ,
- resolution of distance of closest approach to the beam axis less than 250 (100)  $\mu\text{m}$  for tracks with 0.5 (1.7)  $\text{GeV}/c$ . This gives a decay length resolution of about 1 mm for a 100  $\text{MeV}/c^2 A'$ .
- PbWO<sub>4</sub> electromagnetic calorimeter energy resolution  $\Delta E/E \leq 5\%/\sqrt{E}$  and transverse segmentation  $\sim 1.5 \text{ cm}$  (< Moliere radius in PbWO<sub>4</sub>). The energy resolution requirement for triggering is less

---

\*Corresponding author.  
Email address: phansson@slac.stanford.edu (P. Hansson Adrian)

stringent because the electrons and positrons have  $E > 0.5$  GeV. The segmentation provides good spatial resolution and guarantees minimal shower overlap with background hits.

The HPS Test Run apparatus was installed on April 19, 2012, and ran parasitically in the photon beam of the HDice experiment [12] until May 18. The JLab run schedule precluded any dedicated electron beam running, but the HPS Test Run was allowed an eight hour dedicated photon beam run at the end of scheduled CEBAF running. During this dedicated period,  $e^+e^-$  pairs, produced in a gold foil upstream of the experiment, were studied. With no dedicated electron beam running, it was not possible to search for an  $A'$ . However, the final running provided enough data to demonstrate the functionality of the apparatus, document its performance, and explore trigger rates, as shown below.

This paper reviews the HPS Test Run apparatus, documenting the performance of the trigger, data acquisition, silicon tracking and vertex detector, and the electromagnetic calorimeter at, or close to, the level required for the HPS experiment.

## 2. Detector Overview

The HPS Test Run apparatus was designed to run in Hall B at JLab using the CEBAF 499 MHz electron beam at energies between 2.2 and 6.6 GeV and currents between 200 and 600 nA. The overall design of the experiment follows from the kinematics of  $A'$  production which typically results in a final state particle within a few degrees of the incoming beam, especially at low  $m_{A'}$ . Detectors must therefore be placed close to the beam. The intense electron beam enlarges downstream after multiple scattering in the target and electrons which have radiated in the target disperse horizontally in the field of the analyzing magnet. Together they constitute a “wall of flame” which must be completely avoided. Accordingly, the apparatus is split vertically to avoid a “dead zone”, the region within  $\pm 15$  mrad of the beam plane. In addition, the beam is transported in vacuum through the tracker to minimize beam-gas interaction backgrounds. Even with these precautions, the occupancies of sensors near the beam plane are high, dominated by the multiple Coulomb scattering of the primary beam, so high-rate detectors, a fast trigger, and excellent time tagging are required to minimize their impact. The trigger comes from a highly-segmented lead-tungstate ( $PbWO_4$ ) crystal calorimeter located just downstream of the dipole magnet.

A rendering of the apparatus installed on the beam line is shown in Figure 1 and an overview of the coverage, segmentation and performance is given in Table 1.

The silicon tracking and vertexing detector for the HPS Test Run, or SVT, resides in a vacuum chamber inside the Pair Spectrometer (PS) dipole magnet in Hall B at JLab. The magnetic field strength was 0.5 T oriented vertically throughout the run. The SVT has five measurement stations, or “layers,” beginning 10 cm downstream of the target. Each layer comprises a pair of closely-spaced silicon microstrip sensors responsible for measuring a single coordinate, or “view”. Introduction of a small (50 or 100 mrad) stereo angle between the two sensors of each layer provides three-dimensional tracking and vertexing throughout the acceptance of the detector. In order to accommodate the dead zone, the SVT is built in two halves that are approximately mirror reflections of one another about the plane of the nominal electron beam. Each layer in one half is supported on a common support plate with independent cooling and readout.

The electromagnetic calorimeter (ECal) is also split into two halves. Each half of the ECal consists of 221  $PbWO_4$  crystals arranged in rectangular formation. There are five rows with 46 crystals in each row except the row closest to the beam plane which has 37. The light from each crystal is read out by an Avalanche Photodiode (APD) glued on the back surface of the crystal. Signals from the APDs are amplified using custom-made amplifier boards before being sent to the data acquisition electronics.

The Data Acquisition system combines two architectures, the Advanced Telecom Communications Architecture (ATCA) based SVT readout system and VME-bus Switched Serial (VXS) based digitization and triggering system for the ECal.

## 3. The HPS Test Run Beamline

Since an electron beam was unavailable, the HPS Test Run detected the electrons and positrons produced by interactions of the secondary photon beam with a thin foil just upstream of the detectors. The HPS Test Run studied the performance of the detectors and the multiple Coulomb scattering of the electrons and positrons. Figure 2 shows the layout of the setup on the beam line. The SVT was installed inside the Hall B pair spectrometer magnet vacuum chamber with the ECal mounted downstream of it. Both the SVT and the ECal were retracted off the beam plane compared to nominal electron beam running to allow clean passage of the photon beam through the system.

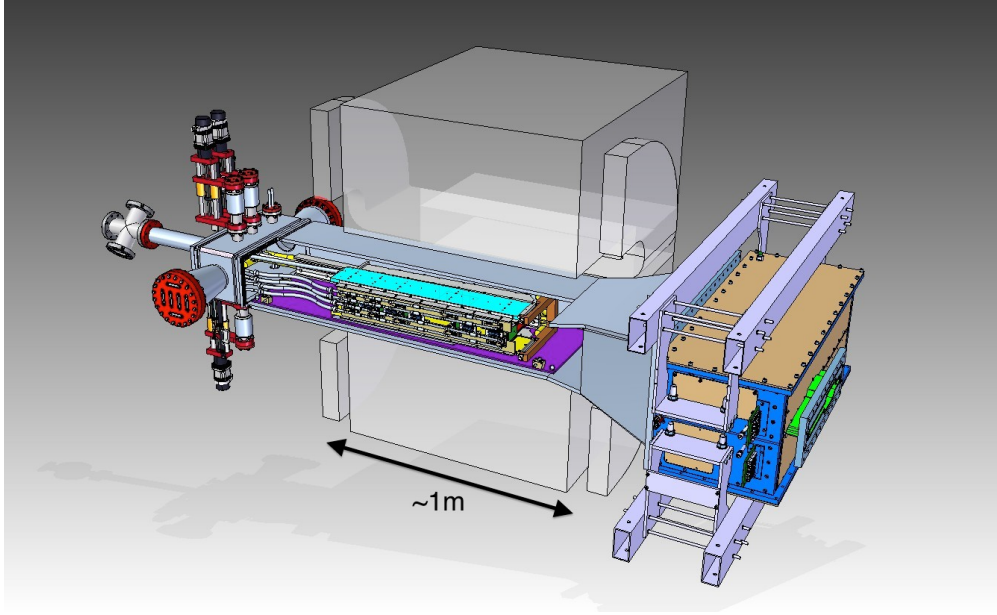


Figure 1: Rendering of the HPS Test Run apparatus installed on the beam line.

Table 1: Overview of the coverage, segmentation and performance of the HPS Test Run detector. The  $\sigma_{d0}$  is the track impact parameter resolution of the SVT at the nominal iron target position.  $\sigma_{pos}$  is the estimated position resolution perpendicular to the strip direction on the silicon sensors of the SVT.

System	Coverage (mrad)	# channels	ADC (bit)	# layers	Segmentation	Time resolution (ns)	Performance
SVT	$15 < \theta_y < 70$ (5 hits)	12780	14	5 (stereo layers)	$30 \mu\text{m}$ (sense) $60 \mu\text{m}$ (readout) ( $\sigma_{pos} \approx 6 \mu\text{m}$ )	2.5	$\sigma_{d0,y} \approx 100 \mu\text{m}$ $\sigma_{d0,x} \approx 300 \mu\text{m}$ $\sigma_{d0,z} \approx 1 \text{ mm}$
ECal	$15 < \theta_y < 60$	442	12	1	$1.33 \times 1.33 \text{ cm}^2$ $1.6 \times 1.6 \text{ cm}^2$	4 (trigger)	$\sigma(E)/E \approx 4.5\%/\sqrt{E}$ Ref. [13, 14, 15]

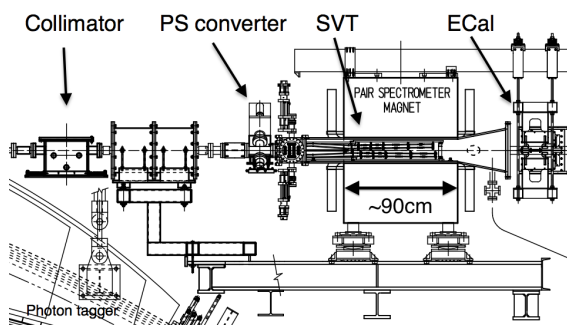


Figure 2: Layout of the HPS parasitic run.

The photon beam was generated in the interaction of 5.5 GeV electrons with a  $10^{-4} X_0$  gold radiator located  $\approx 9$  m upstream of the PS. The primary beam and scattered electrons are deflected away from detectors by the dipole magnet of the photon tagging system. During the dedicated HPS Test Run period, the collimated (6.4 mm diameter) photon beam passes through the PS pair converter gold foil and later the HPS system. The PS pair converter was located  $\approx 77$  cm upstream of the first layer of the SVT.

Data was taken on three different converter thicknesses with photon fluxes between  $0.4-1.3 \times 10^8/\text{s}$  at photon energies between 0.55 and 5.5 GeV produced by a 30-90 nA electron beam. Data was measured for both polarities of the PS dipole magnet. The photon beam line during the HPS Test Run produced a relatively large number of  $e^+e^-$  pairs originating upstream

Converter thickn. (% $X_0$ )	Duration (s)	$e^-$ on radiator ( $\mu\text{C}$ )
0	1279	88.1
0.18	2640	193.5
0.45	2149	140.7
1.6	911	24.4

Table 2: Measured integrated currents for the dedicated photon runs.

of the converter position. This contribution was measured during data taking with “empty” converter runs, i.e. removing the converter but with all other conditions the same. The runs taken during the time dedicated to HPS Test Run are summarized in Table 2.

#### 4. Silicon Vertex Tracker

The Silicon Vertex Tracker (SVT) enables efficient reconstruction of charged particles and precise determination of their trajectories. This allows  $A'$  decays to be distinguished from background via simultaneous measurements of the invariant mass of  $e^+e^-$  decay products and the position of decay vertices downstream of the target.

The design of the SVT is primarily driven by physics requirements and constraints from the environment at the interaction region. The  $A'$  decay products have momenta in the range of 0.4-2.0 GeV/c (for a 2.2 GeV beam), so multiple scattering dominates mass and vertexing uncertainties for any possible material budget. The SVT must therefore minimize the amount of material in the tracking volume. The signal yield for long-lived  $A'$  is very small, so the rejection of prompt vertices must be exceedingly pure, on the order of  $10^{-7}$ , in order to eliminate all prompt backgrounds. To achieve the required vertexing performance the first layer of the SVT must be placed no more than about 10 cm downstream of the target. At that distance, it is found that the active region of a sensor can be placed as close as 1.5 mm from the center of the beam, defining the 15 mrad “dead zone” mentioned previously, to maximize low-mass  $A'$  acceptance with decay products nearly collinear with the beam axis. At the edge of this “dead zone”, the radiation dose approaches  $10^{15}$  electrons/cm<sup>2</sup>/month, or roughly  $3 \times 10^{13}$  1 MeV neutron equivalent/cm<sup>2</sup>/month [16], requiring the sensors to be actively cooled. Meanwhile, very low-energy delta rays from beam-gas interactions would multiply the density of background hits, so the SVT must operate inside the beam vacuum. Finally, in order to protect the sensors, the detector must be movable

so that it can be retracted during periods of uncertain beam conditions or beam tuning.

A mass resolution of 2.5% is adequate to extend a bump-hunt search for an  $A'$  into virgin territory. For running at 2.2 GeV, this translates into a requirement for track momentum ( $p$ ) resolution of 4-5% and angular resolution of about 2 mrad/ $p$ (GeV/c) [11]. Multiple Coulomb scattering dominates both the mass and vertexing uncertainties, relaxing the spatial hit resolution requirement to  $< 100 \mu\text{m}$  ( $50 \mu\text{m}$ ) in the bend (non-bend) plane.

High background occupancies, up to 4 MHz/mm<sup>2</sup> locally, in the region closest to the beam result from beam electrons undergoing multiple scattering in the target. These background hits are rejected by requiring reconstruction of the hit time relative to the trigger with 2 ns resolution.

##### 4.1. Layout

The layout of the SVT is summarized in Table 3 and rendered in Figure 3. Each of the layers is comprised of a pair of closely-spaced silicon microstrip sensors mounted back-to-back to form a module. A 100 mrad stereo angle is used in the first three layers to provide higher-resolution 3D space points for vertexing. Using 50 mrad in the last two layers breaks the tracking degeneracy of having five identical layers and minimizes fakes from ghost hits to improve pattern recognition. Altogether, the SVT has 20 sensors for a total of 12780 readout channels.

Layer	1	2	3	4	5
$z$ from target (cm)	10	20	30	50	70
Stereo angle (mrad)	100	100	100	50	50
Bend res. ( $\mu\text{m}$ )	$\approx 60$	$\approx 60$	$\approx 60$	$\approx 120$	$\approx 120$
Non-bend res. ( $\mu\text{m}$ )	$\approx 6$	$\approx 6$	$\approx 6$	$\approx 6$	$\approx 6$
# of sensors	4	4	4	4	4
Dead zone (mm)	$\pm 1.5$	$\pm 3.0$	$\pm 4.5$	$\pm 7.5$	$\pm 10.5$
Power cons. (W)	6.9	6.9	6.9	6.9	6.9

Table 3: Layout of the SVT.

The SVT is built in two separate halves that are mirror reflections of one another about the plane of the nominal electron beam. Each half consists of five modules mounted on a support plate that provides services to the modules and allows them to be moved as a group relative to the dead zone. The two halves of the tracker are connected to hinges mounted on a C-shaped support

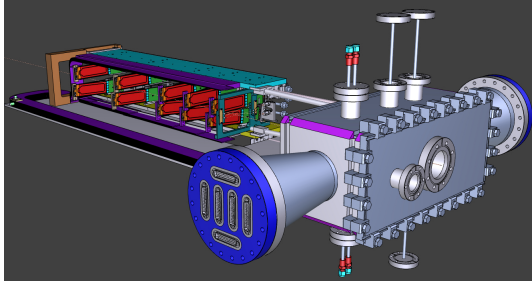


Figure 3: A rendering of the SVT showing the modules on their support plates held by the hinged C-support on the left and the motion levers on the right. The sensors are shown in red and the hybrid readout boards in green. The beam enters from the right through a vacuum box with flanges for services.

just beyond the last layer that defines the nominal spacing between the upper and lower halves of the tracker. A shaft attached to each support plate in front of layer one extends upstream and connects to a linear shift that transfers motion into the vacuum box through bellows to open and close the two halves around the dead zone. The C-support is mounted to an aluminum baseplate that defines the position of the SVT with respect to the vacuum chamber. Figure 4 shows a photograph of both completed detector halves prior to final assembly.



Figure 4: Both halves of the HPS Test Run SVT after final assembly at SLAC. The cooling manifolds and integrated cable runs are clearly seen.

#### 4.2. Components

The sensors for the SVT are  $p+$ -on- $n$ , single-sided, AC-coupled, polysilicon-biased microstrip sensors fabricated on  $<100>$  silicon and have 30 (60)  $\mu\text{m}$  sense (readout) pitch over their  $4 \times 10 \text{ cm}^2$  surface. This sensor technology was selected to match the requirement of  $< 1\% X_0$  per layer, single-hit resolution bet-

ter than 50  $\mu\text{m}$  and tolerance of a radiation dose of approximately  $1.5 \times 10^{14}$  1 MeV neutron equivalent/ $\text{cm}^2$  for a six month run. The sensors, produced by Hamamatsu Photonics Corporation, were originally meant for the cancelled Run 2b upgrade of the DØ experiment [17] which satisfied the requirement that the technology must be mature and available within the time and budget constraints.

Despite having only small spots with very high occupancy (up to 4 MHz/mm<sup>2</sup>) closest to the primary beam, the rates are still high and lowering the peak occupancy to approximately 1% for tracking requires a trigger window and hit time tagging of roughly 8 ns. The ECal readout and trigger described in Sec. 5.3 can achieve such resolution. To reach this performance the sensors for the SVT are readout by the APV25 ASIC developed for the CMS experiment at CERN [18]. The APV25 ASIC can capture successive samples of the shaper output in groups of three at a sampling rate of approximately 40 MHz. By fitting the known  $CR-RC$  shaping curve to these samples, the initial time of the hit can be determined to a precision of 2 ns for S/N≈25 [19]. For electron beam running, six-sample readout and the shortest possible shaping time (35 ns) are used to best distinguish hits that overlap in time. The APV25 ASICs are hosted on simple FR4 hybrid readout boards outside the tracking volume with a short twisted-pair pigtail cable to provide power, configuration, and signal readout. Along with a single sensor, these are glued to a polyimide-laminated carbon fiber composite backing making up a half-module. A window is machined in the carbon fiber leaving only a frame around the periphery of the silicon to minimize material. A 50  $\mu\text{m}$  sheet of polyimide is laminated to the surface of the carbon fiber with 1 mm overhang at all openings to ensure good isolation between the back side of the sensor, carrying high-voltage bias, and the carbon fiber which is held near ground.

The sensor modules for the SVT consist of a pair of identical half-modules, sandwiched back-to-back around an aluminum cooling block at one end and a similar PEEK spacer block at the other. Figure 5 shows a single module after assembly. The cooling block provides the primary mechanical support for the module as well as cooling via copper tubes pressed into grooves in the plates. The spacer block defines the spacing between the sensors at the far end of the module, stiffens the module structure, and improves the stability of the sensor alignment. The average support material in the tracking volume is approximately 0.06%  $X_0$  per double-sided module for a total material budget of 0.7% per layer.

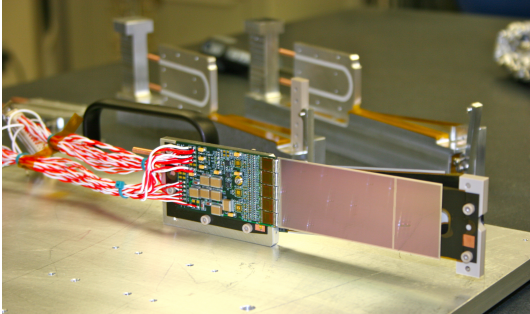


Figure 5: A prototype module assembly (foreground) with the 50 mrad (left) and 100 mrad (right) module assembly fixtures in the background. A pair of cooling blocks and a spacer block can be seen on the fixtures.

The total SVT power consumption budget of about 50 W is removed by a water/glycol mixture circulated through a flexible manifold attached to the copper tubes in the cooling blocks. During the HPS Test Run the sensors were operated at around 23° C. The power consumption is dominated by five APV25 ASICs on each hybrid board consuming approximately 2 W, the radiant heat load is less than 0.5 W per sensor and leakage current is only significant in a small spot after irradiation.

#### 4.3. Production, Assembly and Shipping

Hybrids with APV25 ASICs underwent quick qualification testing and each half-module was run at low temperature ( $\approx 5^\circ \text{C}$ ) and fully characterized for pedestals, gains, noise and time response after assembly. Of 29 half-modules built, 28 passed qualification testing, leaving eight spare modules after completion of the SVT. Only sensors capable of 1000 V bias voltage without breakdown were used. Full-module assembly and mechanical surveys were performed at SLAC before final assembly, testing and shipping of the SVT to JLab. A custom shipping container with nested crates and redundant isolation for shock and vibration was built in order to safely send the partly assembled SVT to JLab. At JLab, the entire SVT was integrated with the full data acquisition and the power supplies before moving the module-loaded support plates to Hall B for final mechanical assembly and installation inside of the vacuum chamber.

#### 4.4. Alignment

The SVT was aligned using a combination of optical, laser and touch probe surveys at SLAC and JLab. The optical survey of individual modules with a precision of

a few  $\mu\text{m}$  was combined with a touch-probe survey of the overall SVT support structure, with 25–100  $\mu\text{m}$  precision, to locate the silicon sensor layers with respect to the support plates and the mechanical survey balls on the base plate. After full assembly and installation of the SVT at JLab, a mechanical survey of the SVT base plate position inside the pair spectrometer vacuum chamber is used to determine the global position of the SVT with respect to the CEBAF beam line. The resulting survey-based alignment has the position of the silicon sensors correct to within a few hundred microns measured from tracks in the HPS Test Run data. A more sophisticated global track-based alignment technique to reach final alignment precision well below 50  $\mu\text{m}$  is being developed.

### 5. Electromagnetic Calorimeter

The electromagnetic calorimeter (ECal), installed downstream of the PS dipole magnet, performs two essential functions for the experiment: it provides a trigger signal to select what events to read out from the detector sub-systems and is used to identify electrons and positrons. The technology and design choices are largely driven by the need for a compact forward design covering the SVT A' acceptance and the ability to measure the energy and positions of electrons and positrons with energy between 0.5 and 6.6 GeV. It needs granularity and signal readout speed to handle 1 MHz/cm<sup>2</sup> of electromagnetic background as well as good radiation hardness. Even modest energy resolution is adequate for triggering. HPS requires better energy resolution,  $\sigma(E)/E < 5\%/\sqrt{E}$ , so that the ECal energy measurement can be used in combination with that from the SVT to improve the overall momentum resolution.

The PbWO<sub>4</sub> crystal inner calorimeter of the CLAS detector [13, 14, 15], in operation since 2005 in Hall B, meets all the requirements set by HPS. The modules from this calorimeter have been subsequently repurposed for HPS.

#### 5.1. Components

The ECal module shown in Figure 6 is based on a tapered 160 mm long PbWO<sub>4</sub> crystal with a 13.3 × 13.3 mm<sup>2</sup> (16 × 16 mm<sup>2</sup>) front (rear) face wrapped in VM2000 multilayer polymer mirror film. The scintillation light yield, approximately 120 photons/MeV, is read out by a 5×5 mm<sup>2</sup> Hamamatsu S8664-55 Avalanche Photodiode (APD) with 75% quantum efficiency glued to the rear face surface using MeltMount 1.7 thermal plastic adhesive. This results in about eight

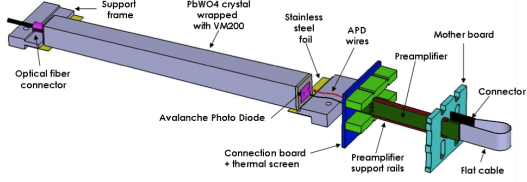


Figure 6: A schematic view of an ECal module.

photoelectrons/MeV which needs to be amplified before being fed into the JLab Flash ADC [20] (FADC) board for digitization and processing. The maximum energy deposited in a crystal is expected to be 4.2 GeV which needs to match the input range of the FADC. The relatively low gain of the APD ( $\sim 200$ ) was compensated with custom-made preamplifier boards, that provide further amplification to match the 2 V dynamic range of the FADC. The ADC has 12-bit resolution. Gains are adjusted to give about 1 ADC count/MeV. This dynamic range is adequate to measure the 10 MeV noise level as well as the the maximum energy expected in a single crystal, about 4 GeV.

## 5.2. Layout

Similar to the SVT, the ECal is built in two separate halves that are mirror reflections of one another about the plane of the nominal electron beam to avoid interfering with the 15 mrad “dead zone”. As shown in Figure 7, the 221 modules in each half, supported by aluminum support frames, are arranged in rectangular formation with five layers and 46 crystals/layer except for the layer closest to the beam where nine modules were removed to allow a larger opening for the outgoing electron and photon beams. Each half was enclosed in a temperature controlled box ( $< 1^\circ \text{ F}$  stability and  $< 4^\circ \text{ F}$  uniformity) to stabilize the crystal light yield and the operation of the APDs and its preamplifiers. Four printed circuit boards mounted on the backplane penetrated the enclosure and were used to supply the  $\pm 5$  V operating voltage for the preamplifiers, 400 V bias voltage to the APDs, and to read out signals from the APDs. Each half of the ECal was divided into 12 bias voltage groups with a gain uniformity of about 20%.

During the HPS Test Run, both halves were held in place by four vertical bars attached to a rail above, placing the front face of the crystals 147 cm from the upstream edge of the magnet, with a 8.7 cm gap between the innermost edge of the crystals in the two halves.

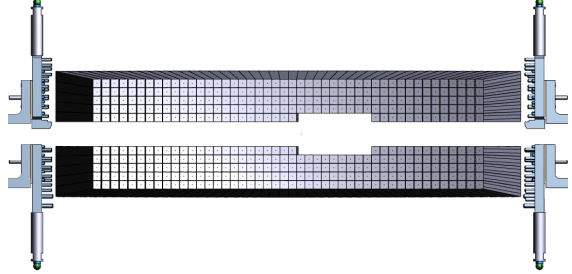


Figure 7: Rendered layout view of the ECal looking downstream.

## 5.3. Signal Readout

After a 2:1 signal splitter, 1/3 of an amplified APD signal was fed to a single channel of a FADC board. 2/3 of the signal was sent to a discriminator module and then to a TDC for a timing measurement. The FADC boards are high speed VXS modules digitizing up to 16 APD signals at 250 MHz and storing samples in 8  $\mu\text{s}$  deep pipelines with 12-bit resolution. When a trigger is received, the part of the pipeline from five samples before and 30 after the signal which crossed a programmable threshold (for the HPS Test Run this was set to  $\approx 70$  MeV) are summed and stored in a 17-bit register for readout. In addition a 4 ns resolution timestamp of the threshold crossing is reported in the readout for each pulse. This scheme significantly compresses the data output of the FADC. During offline data analysis, a calibrated pedestal value is subtracted to obtain the actual summed energy. Two 20-slot VXS crates with 14 (13) FADC boards were employed in the HPS Test Run to read out the top (bottom) half of the ECal.

## 6. Trigger and Data Acquisition

The data acquisition (DAQ) system handles acquisition of data from the ECal and SVT sub-detectors with two DAQ architectures. The SVT DAQ is based on Advanced Telecom Communications Architecture (ATCA) hardware while the ECal uses VMEbus Switched Serial (VXS) based hardware. Data from the sub-detectors are only read out when a trigger signal from the trigger system is received.

### 6.1. Trigger System

The trigger system is designed to select time coincidences of electromagnetic clusters in the top and bottom halves of the ECal which meets kinematic conditions satisfied by  $A'$  decays and minimize backgrounds. The

trigger system needs to be essentially dead-time free, handle rates up to 50 kHz, and supply a trigger signal which jitters < 8 ns from the actual event time in order to minimize backgrounds from out-of-time hits in the SVT. Figure 8 shows a schematic overview of each stage of the system. Each channel on the FADC board has an independent data path to send 5-bit pulse energy and 3-bit pulse arrival time information every 32 ns to a Crate Trigger Processor board (CTP), which is in the same crate. The 3-bit pulse arrival time allows the trigger to know the pulse timing at 4 ns resolution. Contrary to the readout path described in Sec. 5.3, this energy is a pedestal-subtracted time-over-threshold sum with programmable offsets and minimum threshold discriminator for each channel. With input from all FADC channels, i.e. one half of the ECal, the CTP performs cluster finding and calculates cluster energy and timing information. The 3x3 fixed-window, highly parallel, FPGA-based cluster algorithm simultaneously searches for up to 125 clusters with energy sum larger than the programmable energy threshold set to about 270 MeV. This high threshold didn't hurt the trigger rate rate studies for the HPS Test run since only clusters with high energies were studied but for HPS this threshold will need to be lower. Crystals in the fixed-window are included in the sum if the leading edge of the pulse occurred within a 32 ns time window to take into account clock skew and jitter throughout the system. The CTP only accepts clusters with the locally highest energy 3x3 window to deal with overlapping and very large clusters. The Sub-System Processor board (SSP) receives the clusters from the top and bottom half CTP at a maximum rate of 250 MHz and searches for pairs of clusters in an 8 ns wide coincidence window. The SSP sends triggers to the trigger supervisor (TS), which generates all the necessary signals and controls the entire DAQ system readout through the trigger interface units installed in every crate that participate in the readout process.

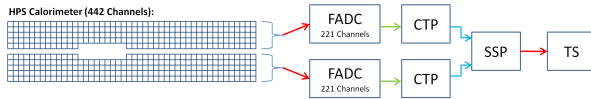


Figure 8: Block diagram of the ECAL trigger system consisting of the FADC that samples and digitizes signals for each detector channel and sends them for cluster finding in the CTP. The CTP clusters are sent to the SSP where the final trigger decision is taken based on pairs of clusters in both halves of the ECal. The decision is sent to the Trigger Supervisor (TS) that generates the necessary signals to read out the sub-detectors.



Figure 9: The SVT DAQ COB board with four data processing daughter cards (DPMs) visible on the left side.

The trigger system is free-running and driven by the 250 MHz global clock and has essentially zero dead time at the occupancies expected for HPS. The trigger supervisor can apply dead time if necessary, for example on a ‘busy’ or ‘full’ condition from the front-end electronics. The system is designed to handle trigger rates above 50 kHz and has a latency set to  $\approx 3 \mu\text{s}$  to match that required by the SVT APV25 ASIC.

During most of the HPS Test Run, the trigger system required only a single cluster in either the top or bottom ECal halves resulting in rates below 2 kHz. However, the trigger system was tested to rates above 100 kHz by lowering thresholds.

## 6.2. SVT Data Acquisition

The purpose of the SVT DAQ is to support the continuous 40 MHz readout and processing of signals from each of the 20 silicon strip sensors of the SVT. The data for each strip channel, six samples of the signal, needs to be transferred to the JLab DAQ for those events selected by the trigger at rates up to 50 kHz and with data transfer rates up to 100 MB/s.

The SVT DAQ is based on the Reconfigurable Cluster Element (RCE) and cluster interconnect concept developed at SLAC as generic building blocks for DAQ systems. The RCE is a generic computational building block, housed on a separate daughter card called Data Processing Module (DPM), that is realized on an ATCA front board called the Cluster On Board (COB), as shown in Figure 9. The first generation RCE used in the HPS Test Run consisted of a Virtex 5 FPGA with 1 GB of DDR3 RAM. A schematic overview of the system is shown in Figure 10. The analog outputs of up to 12 SVT half-modules (60 APV25 ASICs) are digitized on the Rear-Transition-Module (RTM), a custom board on the back side of the ATCA crate, interfacing the HPS-specific readout to the generic DAQ components on the COB. A preamplifier converts the APV25

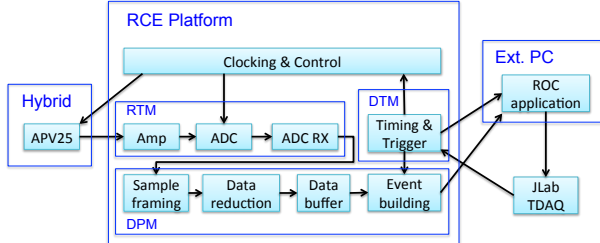


Figure 10: Block diagram overview of the SVT DAQ.

ASIC differential current output to a different voltage output scaled to the sensitive range of a 14-bit ADC operating at the system clock of 41.667 MHz. The RTM is organized into four sections with each section supporting three SVT half-module hybrids (15 APV25 ASICs). The RTM also includes a 4-channel fiber-optic module and supporting logic which is used to interface to the JLab trigger system supervisor. Each section of the RTM is input to a DPM which apply thresholds for data reduction and organizes the sample data into UDP datagrams. The DPM also hosts an I<sup>2</sup>C controller used to configure and monitor the APV25 ASICs. A single ATCA crate with two COB cards was used, one supporting four DPMs and one supporting three DPMs and one DPM that is configured as the trigger and data transmission module. The two COB cards and their DPMs are interconnected with a 10 Gb/s switch card [21] which also hosts two 1 Gb/s Ethernet interfaces to the external SVT DAQ PC.

The external PC supports three network interfaces: two standard 1 Gb/s Ethernet and one custom low-latency data reception card. The first is used for slow control and monitoring of the eight DPM modules and the second serves as the interface to the JLAB data acquisition system. The third custom low-latency network interface is used to receive data from the ATCA crate and supports a low latency, reliable TTL trigger acknowledge interface to the trigger DPM. This PC hosts the SVT control and monitoring software as well as the readout controller application used to interface with the JLab DAQ.

In order to minimize cable length for the analog APV25 ASIC output signal the ATCA crate was located approximately 1 m from the beam line, next to the cable vacuum feed-throughs. Before shielding with lead-blankets and borated polyethylene was arranged, we observed two failures of normally reliable ATCA crate power supplies, time-correlated to beam instabilities.

Although trigger rates during the HPS Test Run were significantly lower, this system was tested at trigger rates up to 20 kHz and 50 MB/s. With optimized event blocking and improved Ethernet bandwidth, together with utilizing the overlapping readout and trigger functionality of the APV25 ASIC, the system is capable of being read out at 50 kHz trigger rate.

### 6.3. General Data Acquisition and Online Computing

Every crate participating in the readout process contains a Readout Controller (ROC) that collects digitized information, processes it, and sends it on to the event builder. For the ECal, both VXS crates run ROC applications in a single blade Intel-based CPU module running CentOS Linux OS. For the SVT DAQ, the ROC application runs on the external PC under RHEL. The event builder assembles information from the ROCs into a single event which is passed to the event recorder that writes it to a RAID5-based data storage system capable of handling up to 100 MB/s. The event builder and other critical components run on multicore Intel-based multi-CPU servers. The DAQ network system is a network router providing 10 Gb/s high-speed connection to the JLab computing facility for long-term storage. For the HPS Test Run, both the SVT and ECal ROC had a 1 Gb/s link to the network router.

## 7. Reconstruction and Performance

While dedicated electron beam was precluded for the HPS Test Run the short dedicated photon beam run allowed the study of some of the key performance parameters for HPS and the trigger rates expected during electron beam running. This section documents the performance and discusses the implications of these results for HPS.

### 7.1. SVT Performance

For the duration of the HPS Test Run all SVT modules and APV25 ASICs were configured to their nominal operating points [22] with all sensors reverse-biased at 180 V. The sensors were operated within a temperature range of 20 – 24°C. Approximately 97% of the 12,780 SVT channels were found to be operating normally; the fraction of dead or noisy channels varied from 2.4% to 4.7% throughout the HPS Test Run. Most of these losses were due to 2-4 misconfigured APV25 ASICs, a known noisy half-module and problems in two particular APV25 ASICs.

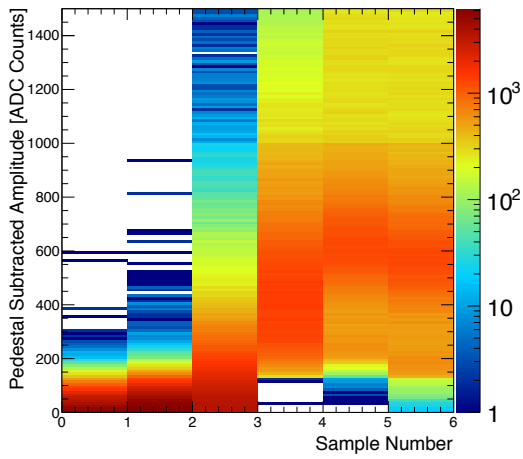


Figure 11: Accumulation of six pedestal-subtracted samples from individual SVT channels associated with hits on tracks.

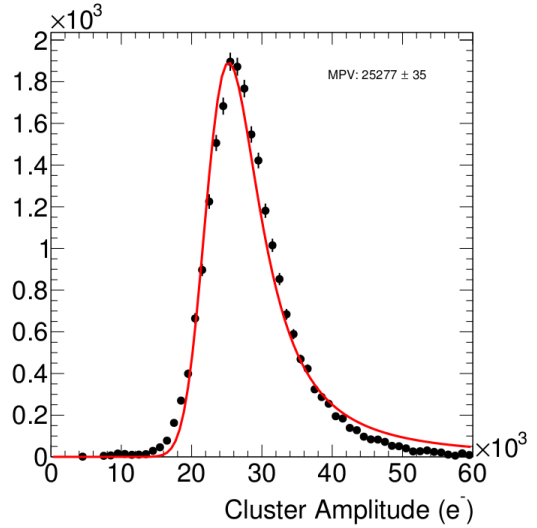


Figure 12: The cluster charge distribution for hits associated with a track follow the characteristic Landau shape.

### 7.1.1. Cluster and Hit Reconstruction

Track reconstruction in the SVT puts stringent requirement on the clustering and hit reconstruction. The multiple scattering in the tracking material dominates the uncertainty in the track parameter estimation and effectively determines the roughly  $50 \mu\text{m}$  ( $100 \mu\text{m}$ ) requirement on the spatial hit resolution in the non-bend (bend) plane. The high occupancy due to multiple scattered beam electrons in the target close to the beam requires a hit time resolution of 2 ns to efficiently reject out-of-time hits in HPS. Both the hit time, based on a fit to the APV25 ASIC pulse shape, and the spatial position reconstruction rely on having  $S/N$  around 25 for the sensors used in HPS.

After a trigger is received, the amplitude of every APV25 ASIC is sampled and digitized in the six consecutive time bins associated with the trigger time. A data reduction algorithm is applied requiring three out of six samples to be above two times the noise level and that the third sample is larger than the second or that the fourth sample is larger than the third. The typical, pedestal subtracted, pulse shape obtained is shown in Figure 11. As the figure demonstrates, the SVT was well timed-in to the trigger with the rise of the pulse at the 3rd sampling point. In order to find the time,  $t_0$ , and amplitude of each hit, the six samples from each channel are fitted to an ideal  $CR - RC$  function. Note that in the HPS Test Run the APV25 ASICs were operating with a 50 ns shaping time. These hits are passed through a simple clustering algorithm which forms clusters by

grouping adjacent strips with the position of a cluster on the sensor determined by the amplitude-weighted mean. With a linear gain up to  $\approx 3$  MIPs, the cluster charge for hits associated with a track follow the characteristic Landau shape, see Figure 12. A noise level between  $1.1 - 1.5 \times 10^3$  electrons was established through multiple calibration runs giving a  $S/N$  of 21 – 25, in line with the requirement for HPS. Radioactive source tests were used to provide the absolute charge normalization. After clustering hits on a sensor, the hit time for each cluster is computed as the amplitude-weighted average of the individually fitted  $t_0$  on each channel. The  $t_0$  resolution is studied by comparing the cluster hit time with the average of all cluster hit times on the track shown in Figure 13. After correcting for offsets from each sensor (time-of-flight and clock phase) and accounting for the correlation between the  $t_0$  and track time, the extracted  $t_0$  resolution is 2.6 ns. This is somewhat worse than the approximately 2 ns resolution expected for  $S/N=25$  which we attribute to the true pulse shape differing from our idealized fit function which will be improved in the future [23]. Reducing the APV25 ASIC pulse shaping time to 35 ns will also improve time resolution. These results show that HPS can operate with the six sample readout mode of the APV25 ASIC and achieve time resolution adequate for pileup rejection during electron running in HPS.

Good agreement was obtained between observed and simulated occupancies after taking into account dead or

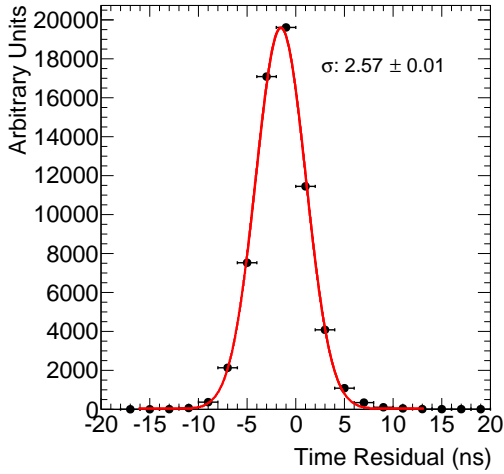


Figure 13: The residual of individual cluster times with the average of all clusters on the track.

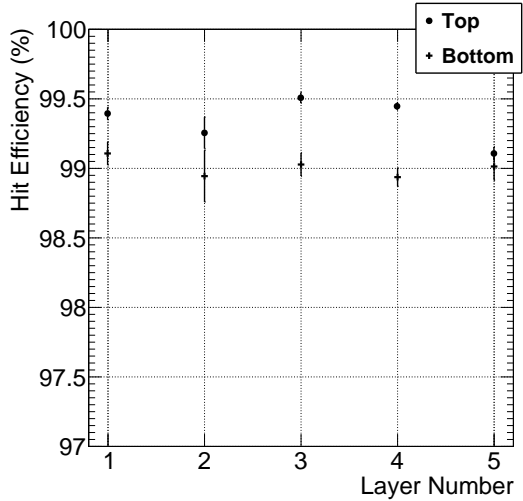


Figure 14: The hit reconstruction efficiency as a function of detector layer.

noisy channels. The hit reconstruction efficiency was estimated by measuring the number of good tracks with a hit close to the interpolated position on a given sensor that was excluded from the track fit. Tracks which intersect regions with known bad channels or pass very close to the edge region were excluded. The hit reconstruction efficiency, see Figure 14, was measured to be above 98% and fairly uniform across the SVT.

The spatial resolution of similar microstrip sensors is well established by test beam data, against which the charge deposition model in the simulation is validated. This resolution can be parameterized as a function of the total signal to single-strip noise and the crossing angle of tracks through the sensor. The single-hit resolution for charged particles with  $S/N > 20$ , as demonstrated here, is relatively constant at approximately  $6 \mu\text{m}$  for tracks that enter approximately normal to the sensors as in HPS. This resolution is significantly better than the requirement for reaching the mass and vertex resolutions required for HPS.

#### 7.1.2. Momentum and Vertexing Resolution

Good track reconstruction performance is crucial to HPS. Simulations show that track momentum resolution of 4-5% is needed to achieve the desired  $A'$  mass resolution. The precise reconstruction of the production vertex to reject prompt QED background requires impact parameter resolutions between 100-250  $\mu\text{m}$  for tracks between 0.5-1.7  $\text{GeV}/c$ . These key performance parameters were studied in the HPS Test Run by selecting

$e^+e^-$  pairs from photon conversions. Pairs of oppositely charged tracks, one in the top and one in the bottom half of the SVT, with momentum larger than 400  $\text{MeV}/c$  were selected and basic distributions of pair production kinematics were studied. The kinematics are relatively well reproduced as shown in Figure 15.

The expected momentum resolution from simulation is between 4-5% for tracks in the momentum range of the HPS Test Run. By comparing the shapes of the kinematic distributions for data and simulation, we estimate an agreement with the nominal scale and resolution to within 10%.

In the HPS Test Run, as well as in electron running with HPS, the dominant source of uncertainty in the tracking and vertexing is multiple Coulomb scattering. For the vertexing performance the foremost difference between the HPS Test Run and HPS is that the HPS Test Run target is 67 cm further upstream, so tracks must be extrapolated nearly eight times as far as in HPS, giving almost collinear tracks in the detector. The increased lever arm over which tracks are extrapolated worsens the resolution up to a factor of eight (depending on momentum) compared to what is achieved at the nominal electron target position for HPS. Figure 16 shows the horizontal and vertical positions of the extrapolated track at the converter position. While residual alignments show small shifts, the good agreement between data and simulated events of the widths indicates a good

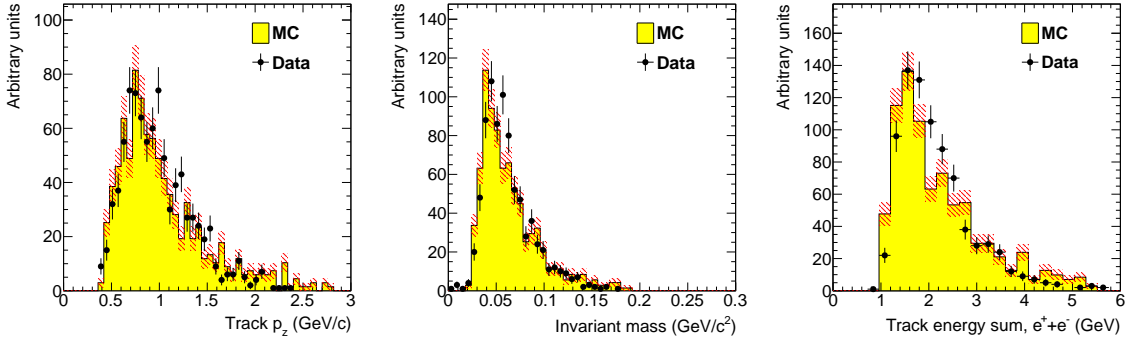


Figure 15: Kinematic distributions for  $e^+e^-$  pairs selected by opposite charged tracks in the top and bottom half of the tracker: track momentum in the top half of the SVT (left), invariant mass (middle) and the sum of the track energy for the pair (right).

understanding of the material budget and distribution in the SVT. Having the dominant contribution to the vertex resolution approximately right demonstrates that the Gaussian part of the vertex resolution in HPS, with a target at 10 cm, will be as calculated.

### 7.2. ECal Performance

During the HPS Test Run 385 out of 442 modules (87%) were used in offline reconstruction, 39 modules were disabled or not read out (no FADC channel available, no APD bias voltage or masked out due to excessive noise) and 18 were masked offline due to noise.

The integrated pulse of each FADC channel was converted to energy by subtracting a pedestal and applying a conversion factor to convert ADC counts to energy. The pedestals are measured using special runs where each trigger records 100 samples of signals from the APDs with 4 ns between each sample. The pedestals were extracted from the part of the window before the actual hit in the calorimeter. Modules with signal above the threshold are clustered using a simple algorithm similar to the one deployed for the trigger (see Sec. 6.1). Due to the high effective crystal readout threshold of 73 MeV the average number of crystals in a cluster was only about three and the simple clustering algorithm worked well for reconstruction of the detected shower energy. An average noise level of approximately 15 MeV per crystal was measured in special pedestal runs. The high crystal noise level and effective threshold didn't hurt the trigger rate studies in the HPS Test Run as clusters with high energy were used for the analysis. For HPS the noise level and threshold will be lowered to improve energy resolution and to allow triggering on cosmics to improve calibration.

The ratio of the ECal cluster energy  $E$  to the momentum  $p$  of a matched track in the SVT was used to de-

termine the conversion factors from ADC counts to energy. To compare data and simulation, all inoperable or noisy channels in the SVT and ECal were disabled in both data and simulation so that any efficiency or bias that affect the data should be reflected in the simulation. Iteratively, conversion coefficients for each crystal were adjusted until the  $E/p$  ratio in data and simulation were similar. The distribution of the  $E/p$  ratio in data and simulation are compared in Figure 17. The peak of the distribution, at  $E/p \sim 0.7$ , gives the sampling fraction of the ECal, the fraction of the incident particle energy measured in the cluster. The width of the distribution indicates the energy resolution, which is worse than the required  $5\%/\sqrt{E}$  for HPS due to high thresholds. The width in data is greater than that in simulation due to non-uniformity of the calibration of different parts of the ECal.

The A' trigger in HPS is relatively insensitive to the energy of the clusters and this level of performance would be adequate. However, improvements are needed to achieve the expected energy resolution in HPS. The noise and thresholds need to be closer to 10 MeV and a more elaborate calibration technique needs to be employed to suppress the large tails in the  $E/p$  distribution further. In addition, the fraction of working channels needs significant improvement.

### 7.3. Trigger Performance

As described above in Sec. 6, the energy from each crystal is determined slightly differently in the trigger and in the readout. The trigger performance was studied by simulating the trigger for each event and comparing to how the events were actually triggered. To eliminate trigger bias, we use a tag and probe method: to study the trigger performance in one half of the ECal, we select events which triggered the other half and where there

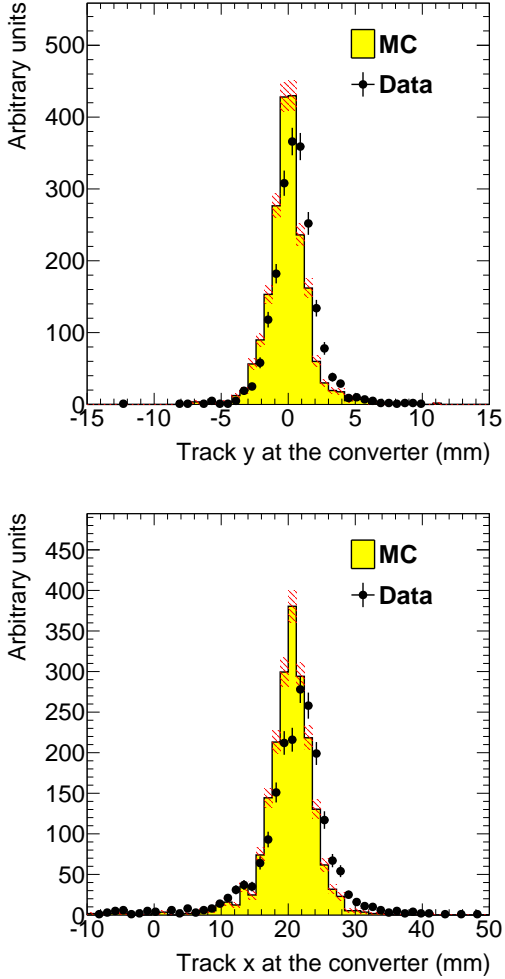


Figure 16: Vertical (top) and horizontal (bottom) extrapolated track position at the converter position taking into account the measured fringe field.

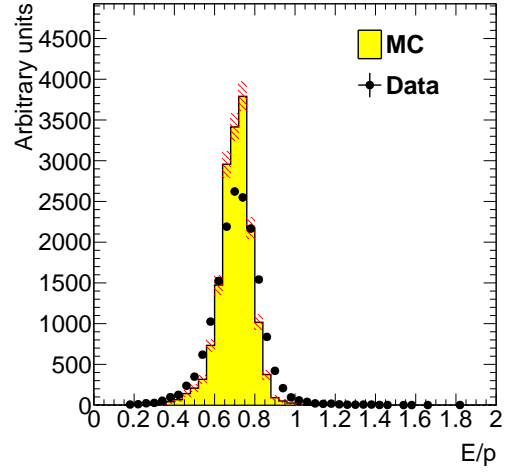


Figure 17: The ECal energy over track momentum ratio ( $E/p$ ) comparing data and simulation for single cluster triggers in the top half of the ECal.

was exactly one probe cluster in the ECal half under study. We then measure trigger efficiency as the fraction of tagged events that fired the trigger in the probe half as a function of the probe cluster energy, shown in Figure 18. The trigger turn-on is slow and reaches an uneven plateau at about 700 MeV for two reasons; gain variations between different crystals lead to the threshold variations and the nonlinearity of the time-over-threshold integral means that the effective threshold is higher for clusters that span multiple crystals. The effective trigger threshold is therefore dependent on position and energy of the particle as well as cluster multiplicity. For HPS the trigger cluster threshold will be set at a lower value.

As a cross-check we simulate the FADC trigger path by converting from readout hits (with fixed-size window integration) to trigger hits (time-over-threshold integration). The CTP clustering algorithm and the trigger decision from the SSP are simulated before we compare the trigger decision and trigger time to what was reported by the actual trigger. For every event, the trigger reports the trigger decision as a bit mask (top half, bottom half or both) and the time the trigger fired. The turn-on from the trigger threshold was measured to be 1280 in units of ADC counts as expected. The threshold was not perfectly sharp because of uncertainties in the conversion from readout to trigger hits described above, but based on comparisons with simulation we found that the trigger worked exactly as specified.

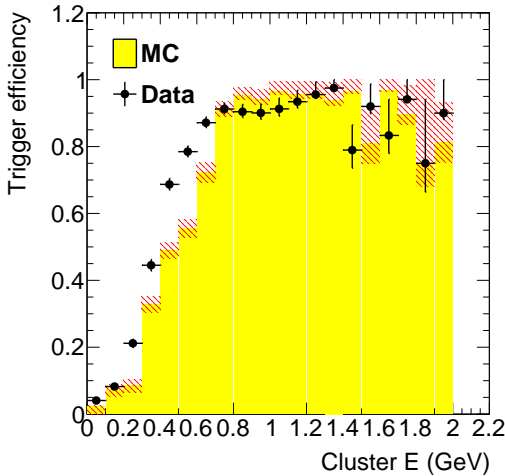


Figure 18: Trigger efficiency in both halves of the ECal for data and simulation as a function of cluster energy.

Converter (% $X_0$ )	<b>1.60</b>	<b>0.45</b>	<b>0.18</b>
EGS5	$1162 \pm 112$	$255 \pm 28$	$94 \pm 17$
Geant4	$2633 \pm 250$	$371 \pm 38$	$114 \pm 18$
Observed	$1064 \pm 2$	$196 \pm 1$	$92 \pm 1$

Table 4: Observed and predicted event rate (in Hz) normalized to 90 nA for three different converter thicknesses. The uncertainty on the prediction includes systematic uncertainties from ECal alignment, background normalization, beam current normalization and limited statistics in the simulation.

#### 7.4. Trigger Rate Comparisons

Trigger rates observed in the HPS Test Run are dominated by  $e^+e^-$  pairs produced in the converter. In simulated events, the rate of triggers depend on the modeling of the pairs' angular distribution and the subsequent multiple Coulomb scattering in the converter. Rates from different converter thicknesses are used to study the varying multiple Coulomb scattering contribution (pair production angular distribution is constant). These rates are compared with those predicted by the standard Geant4 [24] approximation for multiple scattering and the more accurate model used by EGS5 [25]. Restricting to a well calibrated region of the ECal and to clusters with energy above the trigger turn-on, we see agreement with the rates predicted by the EGS5 simulation program after subtracting the “no converter” background , see Table 4. This gives further confidence that the dominant source of background occupancy for HPS, multiple Coulomb scattered beam electrons, is well described.

## 8. Summary and Outlook

The HPS Test Run experiment, using a simplified version of the apparatus planned for the full HPS experiment in a parasitic photon beam, demonstrated the feasibility of the detector technologies proposed for the silicon vertex tracker, electromagnetic calorimeter, and data acquisition systems. Performance from each of these subsystems has been shown to be adequate to conduct the full experiment successfully with some identified improvements. Studies of multiple Coulomb scattering tails of electrons and positrons from photon conversions further backs expectations from simulation, giving credence to estimates of the detector backgrounds expected in electron beam running for HPS.

## 9. Acknowledgements

The authors are grateful for the support from Hall B at JLab and especially the Hall B engineering group for support during installation and decommissioning. They also would like to commend the CEBAF personnel for good beam performance, especially the last few hours of operating CEBAF6. The tremendous support from home institutions and supporting staff also needs praise from the authors.

This work has been supported by the US Department of Energy, the National Science Foundation, French Centre National de la Recherche Scientifique and Italian Istituto Nazionale di Fisica Nucleare. Rouven Essig is supported in part by the Department of Energy Early Career research program DESC0008061 and by a Sloan Foundation Research Fellowship. Authored by Jefferson Science Associates, LLC under U.S. DOE Contract No. DE-AC05-06OR23177.

## References

- [1] B. Holdom, Two U(1)'s and Epsilon Charge Shifts, Phys.Lett. B166 (1986) 196.
- [2] P. Galison, A. Manohar, TWO Z's OR NOT TWO Z's?, Phys.Lett. B136 (1984) 279.
- [3] R. Essig, J. A. Jaros, W. Wester, P. H. Adrian, S. Andreas, et al. (Report of the Community Summer Study 2013 (Snowmass) Intensity Frontier New, Light, Weakly-Coupled Particles subgroup), Dark Sectors and New, Light, Weakly-Coupled Particles, 2013. URL: <http://arxiv.org/abs/arXiv:1311.0029>.
- [4] M. Pospelov, Secluded U(1) below the weak scale, Phys.Rev. D80 (2009) 095002.
- [5] O. Adriani, et al. (PAMELA Collaboration), An anomalous positron abundance in cosmic rays with energies 1.5-100 GeV, Nature 458 (2009) 607–609.

- [6] M. Ackermann, et al. (Fermi LAT Collaboration), Measurement of separate cosmic-ray electron and positron spectra with the Fermi Large Area Telescope, *Phys.Rev.Lett.* 108 (2012) 011103.
- [7] M. Aguilar, et al. (AMS Collaboration), First Result from the Alpha Magnetic Spectrometer on the International Space Station: Precision Measurement of the Positron Fraction in Primary Cosmic Rays of 0.5350 GeV, *Phys.Rev.Lett.* 110 (2013) 141102.
- [8] N. Arkani-Hamed, D. P. Finkbeiner, T. R. Slatyer, N. Weiner, A Theory of Dark Matter, *Phys.Rev.* D79 (2009) 015014.
- [9] M. Pospelov, A. Ritz, Astrophysical Signatures of Secluded Dark Matter, *Phys.Lett.* B671 (2009) 391–397.
- [10] J. D. Bjorken, R. Essig, P. Schuster, N. Toro, New Fixed-Target Experiments to Search for Dark Gauge Forces, *Phys.Rev.* D80 (2009) 075018.
- [11] A. Grillo, et al. (HPS Collaboration), Heavy Photon Search Proposal, 2010. URL: [https://confluence.slac.stanford.edu/download/attachments/86676777/HPSProposal-FINAL\\_Rev2.pdf](https://confluence.slac.stanford.edu/download/attachments/86676777/HPSProposal-FINAL_Rev2.pdf).
- [12] A. Sandorfi, et al., 2012. URL: [http://www.jlab.org/exp\\_prog/proposals/06/PR06-101.pdf](http://www.jlab.org/exp_prog/proposals/06/PR06-101.pdf).
- [13] F.-X. Girod, M. Garon (CLAS), Inner calorimeter in clas/dvcs experiment, CLAS-Note 2005-001 (2005).
- [14] R. Niyazov, S. Stepanyan (CLAS), Clas/dvcs inner calorimeter calibration, CLAS-Note 2005-021 (2005).
- [15] F.-X. Girod (Universite de Strasbourg), 2006. URL: <http://www.jlab.org/Hall-B/general/thesis/fxggirod.pdf>.
- [16] I. Rashevskaya, S. Bettarini, G. Rizzo, L. Bosisio, S. Dittongo, et al., Radiation damage of silicon structures with electrons of 900-MeV, *Nucl. Instrum. Meth.* A485 (2002) 126–132.
- [17] D. S. Denisov, S. Soldner-Rembold, D0 Run IIB Silicon Detector Upgrade: Technical Design Report (2001).
- [18] M. French, L. Jones, Q. Morrissey, A. Neviani, R. Turchetta, et al., Design and results from the APV25, a deep sub-micron CMOS front-end chip for the CMS tracker, *Nucl.Instrum.Meth.* A466 (2001) 359–365.
- [19] M. Friedl, C. Irmler, M. Pernicka, Readout of silicon strip detectors with position and timing information, *Nucl.Instrum.Meth.* A598 (2009) 82–83.
- [20] H. Dong, et al., Integrated tests of a high speed VXS switch card and 250 MSPS flash ADCs, 2007. doi:10.1109/NSSMIC.2007.4436457.
- [21] R. Larsen, Emerging New Electronics Standards for Physics, *Conf.Proc.* C110904 (2011) 1981–1985.
- [22] L. Jones, APV25-S1: User guide version 2.2, RAL Microelectronics Design Group, 2011.
- [23] M. Friedl, C. Irmler, M. Pernicka, Obtaining exact time information of hits in silicon strip sensors read out by the APV25 front-end chip, *Nucl. Instrum. Meth.* A572 (2007) 385 – 387.
- [24] S. A. et al., GEANT4 - a simulation toolkit, *Nucl.Instrum.Meth.* A506 (2003) 250 – 303.
- [25] H. Hirayama, Y. Namito, A. Bielajew, S. Wilderman, W. Nelson, The EGS5 Code System, 2005.